

TiO₂–MoS₂ hybrid nano composites with 3D network architecture as binder-free flexible electrodes for lithium ion batteries

Yingjie Zhang¹ · Shaobo Zhao¹ · Xiaoyuan Zeng¹ · Jie Xiao¹ · Peng Dong¹ · Jinbao Zhao² · Shigang Sun² · Ling Huang² · Xue Li¹

Received: 20 January 2017 / Accepted: 2 March 2017 / Published online: 14 March 2017
© Springer Science+Business Media New York 2017

Abstract TiO₂ hybrid nano composites are encouraging electrode materials for lithium-ion batteries due to the increased specific capacity and excellent electrochemical performance. In this work, the TiO₂–MoS₂ hybrid binder free electrodes have been successfully synthesized by using a facile hydrothermal process. Encouragingly, when being assessed as an anode electrode for LIBs, the MoS₂–TiO₂ electrode after the calcination treatment could retain a capacity of 361.5 mAh g⁻¹ with high capacity retention of 88.0% after 300 cycles at a high current density of 800 mA g⁻¹. Such good performance may be derived from the special 3D network architecture, well-dispersed MoS₂ nanoparticles and the close connection between TiO₂ and MoS₂ after the calcination treatment.

1 Introduction

Titanium dioxide (TiO₂) is considered as the candidate to instead of carbonaceous anodes in Li-ion batteries due to the inherently safety and chemically compatibility with the electrolyte. Compared with the commercialized graphitic carbon anode materials, titanium dioxide is a low cost material with low volume change and high safety [1]. Moreover, the anatase TiO₂ presents a relatively high lithium intercalation/deintercalation voltage, thereby the formation of SEI and electroplating of lithium can be avoided [2, 3]. Besides, the anatase TiO₂ exhibits excellent reversibility and Li-ion mobility, which is attributed to its inherently structural stability [4]. These features make it a promising anode material for advanced energy storage batteries.

However, titanium dioxide has a poor electronic conductivity due to the empty Ti3d-states with a band gap energy of 2–3 eV for tetravalent Ti [5, 6], which may give a moderate rate performance for high power batteries. Apart from this, the limited lithium insertion for TiO₂ restricts the specific capacity. To date, the most common strategies for improving TiO₂ electrochemical performance are (1) synthesize nanostructural TiO₂ materials to accelerate lithium ion diffusion [7–10]; (2) structural doping [9]; and (3) combine well with high electronic conductive materials to improve conductivity [11–13].

In this work, we firstly report an important advance in the development of the TiO₂–MoS₂ hybrid binder-free flexible electrode with a 3D network architecture and enhanced electrochemical performance for lithium ion batteries. More importantly, we have found the calcination treatment can largely improve the electrochemical performance of the hybrid electrode. And the effect of the calcination on the structure stability and electrochemical properties of the

Electronic supplementary material The online version of this article (doi:10.1007/s10854-017-6697-9) contains supplementary material, which is available to authorized users.

✉ Xue Li
438616074@qq.com

¹ National and Local Joint Engineering Laboratory for Lithium-ion Batteries and Materials Fabrication Technology, Yunnan Provincial Laboratory for Advanced Materials and Batteries Application, Faculty of Metallurgical and Energy Engineering, Kunming University of Science and Technology, Kunming 650093, Yunnan, China

² State Key Laboratory of Physical Chemistry of Solid Surfaces, Collaborative Innovation Center of Chemistry for Energy Materials, College of Chemistry and Chemical Engineering, Xiamen University, Xiamen 361005, China

TiO₂–MoS₂ hybrid electrode for LIBs is also discussed in detail.

2 Experimental section

2.1 Material preparation

A piece of clean Ti substrates (with the thickness of 0.05 mm, 99.5% in purity) was transferred into the 100 mL Teflon-lined stainless steel autoclave with 10 mL ethanol and 80 mL of 0.5 M NaOH solution. The sealed autoclave was heated to 220 °C and maintained for 16 h (with a heating rate of 3 °C min⁻¹). After washing with deionized water several times, the precursor was treated with ion exchange to achieve of Na⁺ into H⁺ in 100 mL of 0.1 M HCl for 6 h. Finally, the as-prepared hydrogen titanate was heated to 400 °C for 4 h (with a temperature ramp of 3 °C min⁻¹). Then the pristine TiO₂ electrode grown on Ti substrates was obtained.

In the following synthesis, sodium molybdate (0.06 g) and thiourea (0.12 g) were added to 60 ml deionized water to form a homogeneous solution under constant stirring for 10 min. This solution was placed in a 100 mL Teflon-sealed autoclave, which was maintained at 180 °C for 24 h. Then the solution was filtered and dried under vacuum at 80 °C for 10 h (The obtained sample named as uncalcined TiO₂–MoS₂ electrode). The sample with the calcination treatment was operated in H₂(3%)/Ar(97%) mixture atmosphere at 500 °C for 4 h. The final electrode was obtained when the sample cools to room temperature. (named as calcined TiO₂–MoS₂ electrode hereafter).

2.2 Materials characterizations

Powder X-ray diffraction patterns were tested on a Rigaku MiniFlex600 X'pert. Morphologies of the samples were examined with HITACHI S-4800 and JEM-2100. Area's Energy Dispersive Spectra were conducted using an energy dispersive X-ray device attached to a HITACHI S-4800 SEM. The elemental contents of the prepared material were detected by inductively coupled plasma technique. The X-ray photoelectron spectroscopy analysis was performed with a QUANTUM 2000 SCANNING ESCA MICRO-PROBE spectrometer.

2.3 Electrochemical performance characterization

The electrochemical performance was characterized in CR2016 coin cells with Celgard 2400 (Celgard, Inc., USA) as the separator, and 1 mol L⁻¹ LiPF₆ in a 1:1:1 (V: V: V) mixture of EC, DMC and DEC as the electrolyte. Galvanostatic charge/discharge experiments were

performed at different current densities between 0.02 and 3.0 V (vs Li/Li⁺) by using Land battery test system (LAND-V34, Land Electronic Co., Ltd., Wuhan). The electrochemical impedance spectroscopy were tested by Metrohm Autolab (PGSTAT302N).

3 Results and Discussion

The XRD patterns of TiO₂, uncalcined and calcined MoS₂–TiO₂ electrodes are shown in Fig. 1. Both TiO₂ and uncalcined MoS₂–TiO₂ electrodes just show the characteristic peaks of anatase crystalline form of TiO₂ (JCPDS No. 89-4921) [14, 15], which are found at 2θ = 25.4°, 37.8°, 48.1°, 62.8°, 76.2° except that these diffraction positions at 2θ = 40.2°, 53.0°, 70.6° belong to the metal titanium current collector (JCPDS No. 89-2762). For calcined MoS₂–TiO₂ electrodes, three small and broad peaks can be found at 14°, 33° and 59°. According to the literature, such peaks are related to the (002), (100) and (110) crystallographic planes [16]. It's obvious that the loading of MoS₂ on TiO₂ materials via the hydrothermal process would be successful and effective. Especially after the calcination treatment, MoS₂ with a higher degree of crystallinity can be obtained. And there is not any negative impact on the crystallinity and purity of the TiO₂ during the MoS₂ deposit reaction.

Figure 2 shows SEM and magnified SEM images of TiO₂, uncalcined and calcined MoS₂–TiO₂ electrodes. As shown in Fig. 2a, b, the as-prepared TiO₂ samples show a nano-network structure, composed of nondirectional nanowires, which column diameter is around 20–30 nm. After the MoS₂ deposit reaction, we can clearly see that

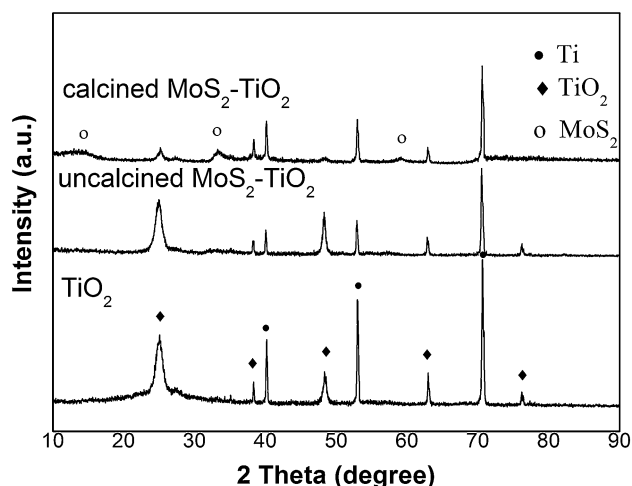
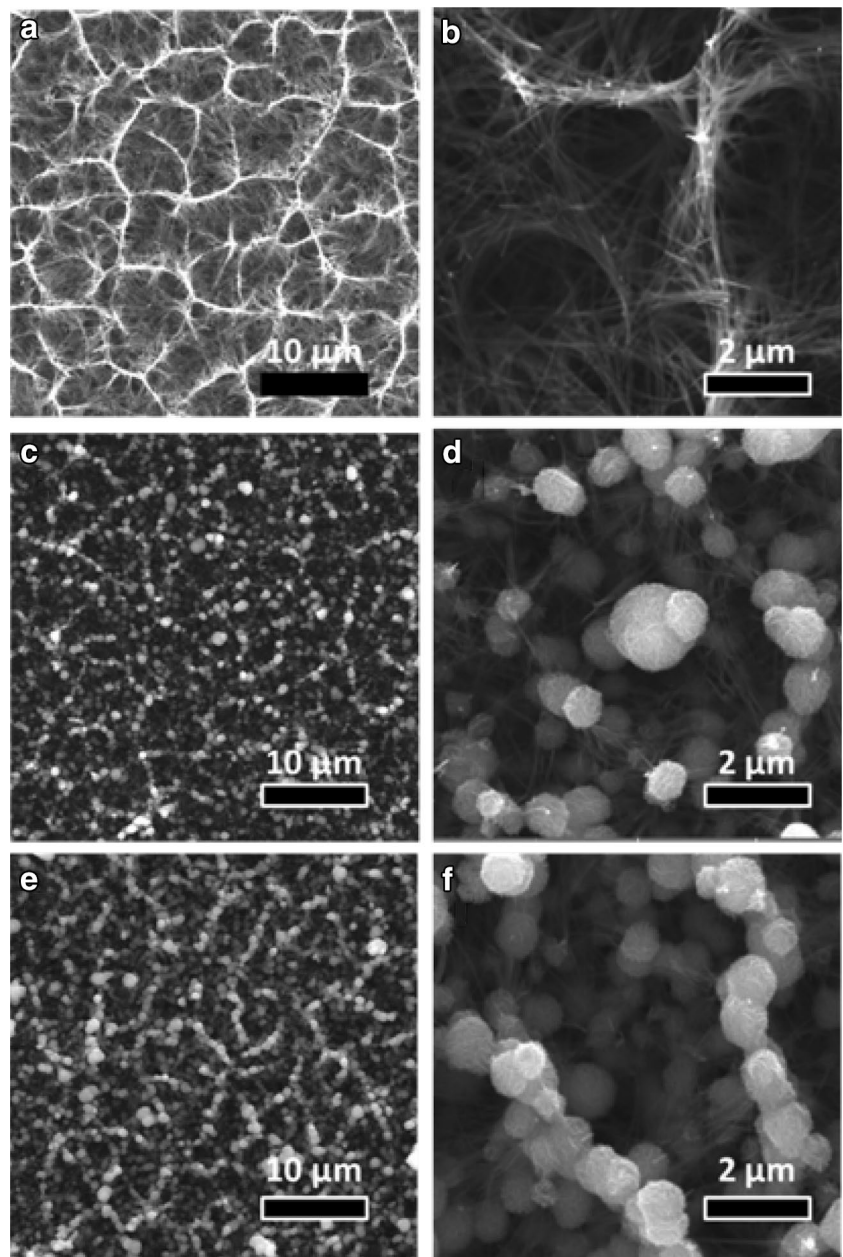


Fig. 1 XRD patterns of TiO₂, uncalcined and calcined MoS₂–TiO₂ electrodes

Fig. 2 SEM and magnified SEM images of **a, b** TiO₂, **c, d** uncalcined MoS₂-TiO₂ and **e, f** calcined MoS₂-TiO₂ electrodes



MoS₂ nanoparticles are successfully adhered to the surface of TiO₂ nano-network structure (Fig. 2c–f). For the calcined MoS₂-TiO₂ electrode, the MoS₂ nanoparticles are liable to deposit not only on the single TiO₂ nanowires but also on the joint of TiO₂ nanowires. In addition, compared with the uncalcined MoS₂-TiO₂ electrode, the calcined MoS₂ contact each other more tightly with a uniform diameter of 1 μm. Finally the more integrated and uniform conductive network can be formed for the calcined MoS₂-TiO₂ electrode.

For the XPS results (Fig. 3a, b), we could find that the major element compositions of the prepared materials are Mo, Ti, O and S. According to the measured results as

shown in Table 1, the mol ratio of S and Mo are determined to be 2.70 and 2.15 for the uncalcined and calcined samples, respectively. Compared with the uncalcined sample, the ratio of Mo and S element for the calcined sample is much closer to the stoichiometric ratio. This indicates the unnecessary sulfur can be removed and the purity of MoS₂ can be improved by the calcination treatment.

In order to further investigate the loading content of MoS₂ on the TiO₂ electrode, the ICP-AES analysis was carried out and the results are listed in Table 2. In accordance with the elemental ratio, the theoretical capacities are calculated as 633 and 651 mAh g⁻¹ for uncalcined and calcined MoS₂-TiO₂ electrodes, respectively [17]. (The

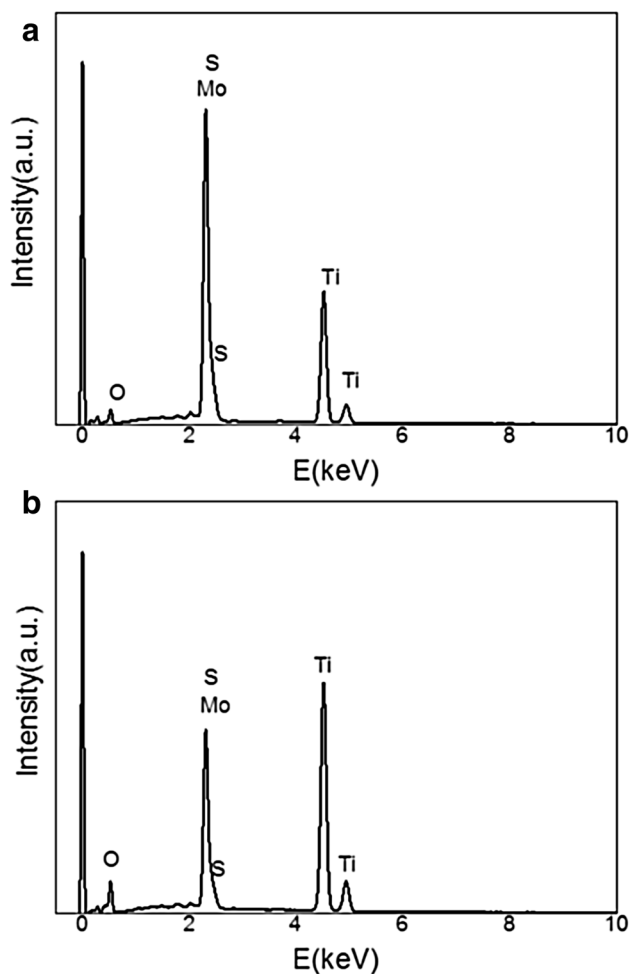


Fig. 3 EDS spectra of **a** uncalcined and **b** calcined $\text{MoS}_2\text{-TiO}_2$ electrodes

Table 1 Elemental contents (in mol percent) of S and Mo in the $\text{MoS}_2\text{-TiO}_2$ samples obtained via EDS analysis

Element	Uncalcined sample	Calcined sample
S	2.70	2.15
Mo	1.00	1.00

Table 2 Elemental mol ratio of Ti and Mo in the $\text{MoS}_2\text{-TiO}_2$ samples obtained via the ICP testing method

Element	Uncalcined sample	Calcined sample
Ti	1.00	1.00
Mo	1.17	1.21

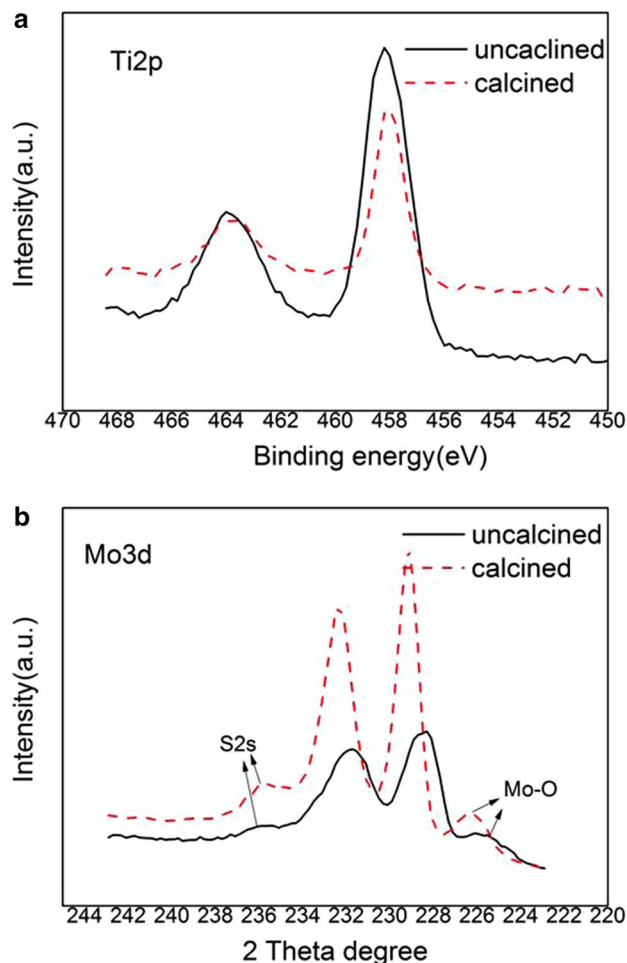


Fig. 4 **a** XPS analysis of $\text{Ti } 2p_{3/2-1/2}$ for $\text{MoS}_2\text{-TiO}_2$ samples, **b** XPS analysis of $\text{Mo } 3d$ for $\text{MoS}_2\text{-TiO}_2$ samples

theoretical capacity of TiO_2 is 335 mAh g^{-1} and that of MoS_2 is 669 mAh g^{-1} .

To investigate the binding states of prepared $\text{MoS}_2\text{-TiO}_2$ samples, high-resolution XPS was used to indicate the $\text{Ti } 2p$ and $\text{Mo } 3d$ core levels (Fig. 4; Table 3). The XPS $\text{Ti } 2p$ peaks corresponding to uncalcined $\text{MoS}_2\text{-TiO}_2$ show a unique doublet at $458.8\text{--}464.4 \text{ eV}$, associated with tetravalent Ti based on TiO_2 [18]. Compared with the uncalcined sample, we observe the XPS $\text{Ti } 2p$ peaks corresponding to the calcined $\text{MoS}_2\text{-TiO}_2$ shift to lower binding energy, which is assigned to the presence of Ti-O-S bonds [19]. The $\text{Mo } 3d$ peaks located at around 236 eV can be found for both the $\text{MoS}_2\text{-TiO}_2$ samples, which belong to the oxidized molybdenum forms [20]. By comparison, the uncalcined sample shows a higher peak of Mo-O than that of the calcined sample, which indicates the MoS_2 contact TiO_2 more tightly after calcination. Both the $\text{MoS}_2\text{-TiO}_2$ samples show a peak at about 226 eV corresponding to the Mo-S bond [21]. For the calcined $\text{MoS}_2\text{-TiO}_2$ sample,

Table 3 Binding energy and assignment of components derived from XPS spectra of MoS₂-TiO₂ samples shown in Fig. 4

Sample	Identity	Binding energy (eV)	Assignment
Uncalcined	Ti 2p _{3/2}	458.2	TiO ₂
	Ti 2p _{1/2}	464.0	TiO ₂
	Mo 3d _{5/2}	228.4	MoS ₂
	Mo 3d _{5/2}	231.8	MoS ₃
	Mo 3d _{3/2}	235.7	Mo-O
	S 2 s	225.8	MoS ₂
Calcined	Ti 2p _{3/2}	458.0	Ti-O-S
	Ti 2p _{1/2}	463.7	Ti-O-S
	Mo 3d _{5/2}	229.2	MoS ₂
	Mo 3d _{5/2}	235.7	Mo-O
	Mo 3d _{3/2}	232.3	Mo-O-S
	S 2 s	226.3	MoS ₂

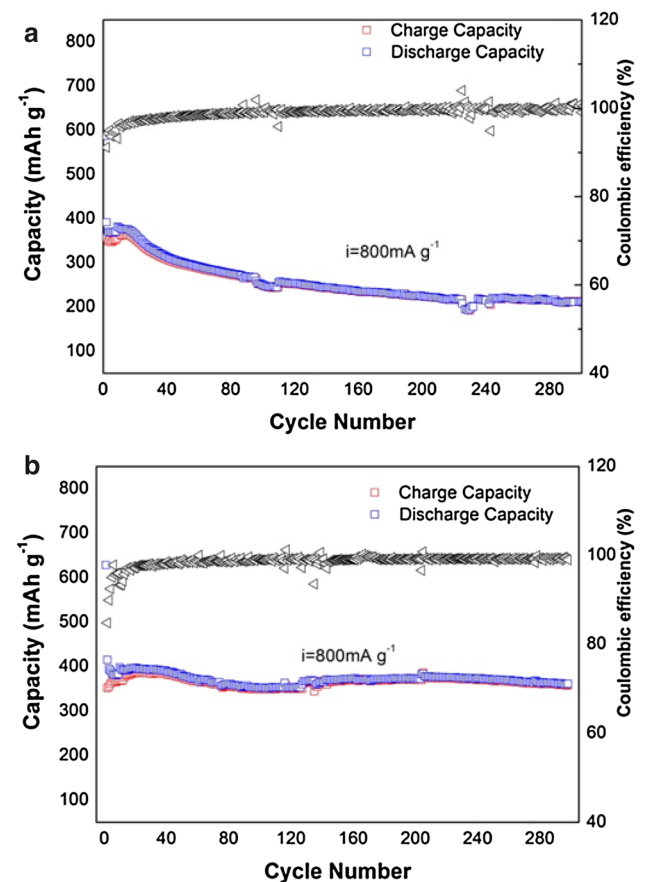


Fig. 5 Cycle performances for **a** uncalcined and **b** calcined MoS₂-TiO₂ electrodes at a current density of 800 mA g⁻¹

the XPS peaks related to the MoS₂ bonds are much higher than that of the uncalcined sample, which due to the higher purity and crystallinity of the MoS₂ obtained after the calcination post-treatment. Moreover, there is a new peak

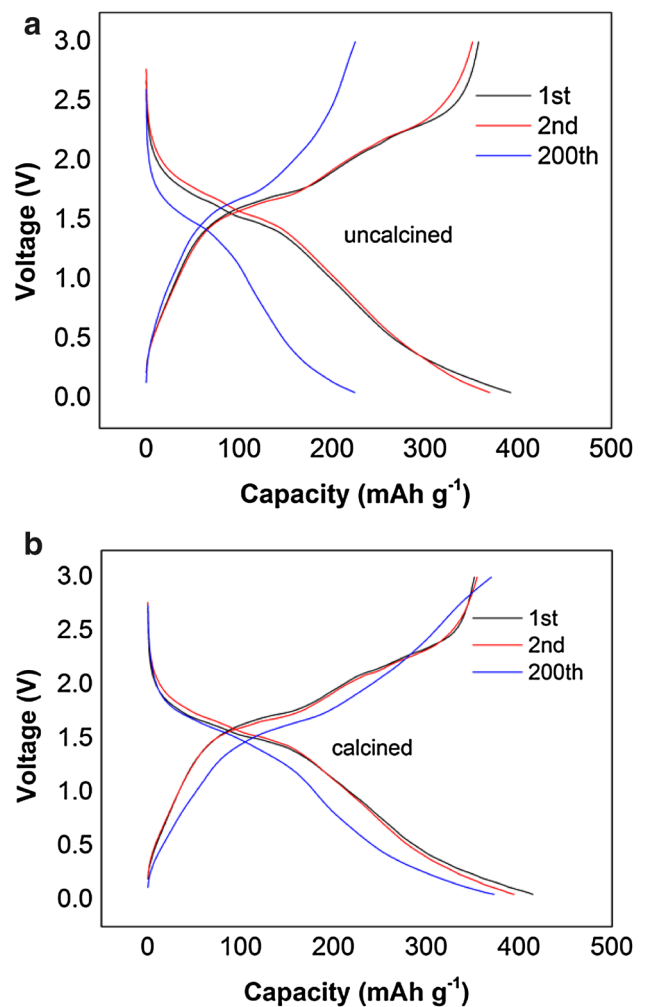


Fig. 6 Charge and discharge curves of **a** uncalcined and **b** calcined MoS₂-TiO₂ electrodes at a current density of 800 mA g⁻¹

corresponding to the Mo-O-S for the calcined MoS₂-TiO₂ sample [20]. This further indicates the MoS₂ contact TiO₂ more tightly after the calcination treatment. The specific capacity and coulombic efficiency with respect to cycle numbers for the uncalcined and calcined MoS₂-TiO₂ electrodes at a high current density of 800 mA g⁻¹ in a half cell are shown in Fig. 5. In terms of the uncalcined MoS₂-TiO₂ electrode, the second discharge capacity is 388.4 mA h g⁻¹ and decreases to 211.5 mA h g⁻¹ after 300 cycles with capacity retention of 54.4%. However, for the calcined MoS₂-TiO₂ electrode, it delivers 361.5 mA h g⁻¹ with high capacity retention of 88.0% after 300 cycles, indicating the remarkable cycling stability.

A comparison of the potential profiles and differential capacity curves for the uncalcined and calcined MoS₂-TiO₂ electrodes are shown in Figs. 6 and 7. Both the samples display the specific electrochemical behaviour of TiO₂ and MoS₂. There are specific voltage platform

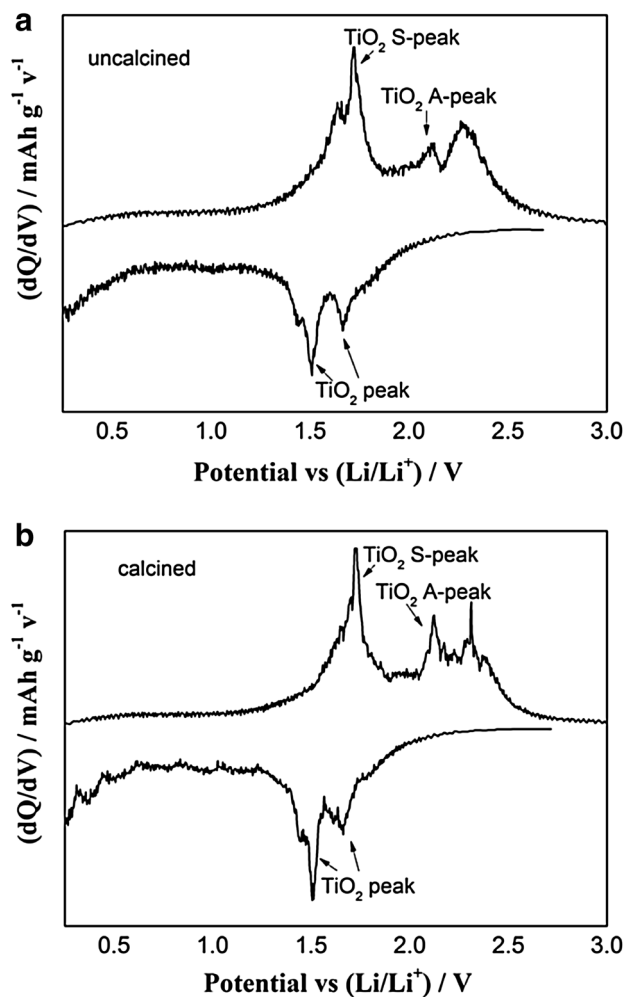


Fig. 7 Differential capacity curves of **a** uncalcined and **b** calcined $\text{MoS}_2\text{-TiO}_2$ electrodes at a current density of 800 mA g^{-1} for the first cycle

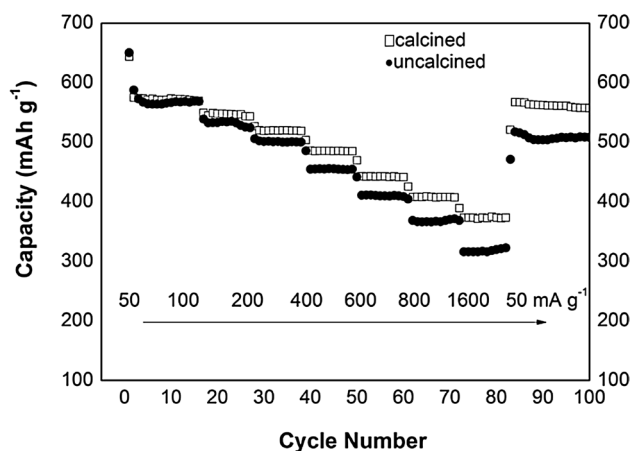


Fig. 8 Rate capabilities of uncalcined and calcined $\text{MoS}_2\text{-TiO}_2$ electrodes at different current densities

observed at 1.75 and 2.0 V during Li^+ insertion and extraction assigned to the TiO_2 nanowires. According to the relational reports, there are three regions of the Li^+ insertion process for TiO_2 [22, 23]. The first potential region is from the open-circuit voltage to 1.75 V forming a solid solution phase, which is depended on Li insertion into the $I4_1/amd$ tetragonal anatase lattice (Li_xTiO_2) [23, 24]. The second voltage region is the platform at 1.75 V, which belongs to a two-phase reaction between the Li-poor tetragonal anatase Li_xTiO_2 and orthorhombic $\text{Li}_{0.5}\text{TiO}_2$ phases [25–27]. The remaining long slope-like potential region represents the non-faradaic process which is similar to the capacitive behavior of nanomaterial [25].

According to the differential capacity curves, there are two couples of oxidation–reduction peaks. The cathodic/anodic peaks (named A-peaks) located at 1.75 and 2.0 V represent the solid-state lithium ion insertion/extraction process in the anatase TiO_2 lattice. And the other cathodic/anodic peaks (named S-peaks) located at 1.55 and 1.65 V represent the

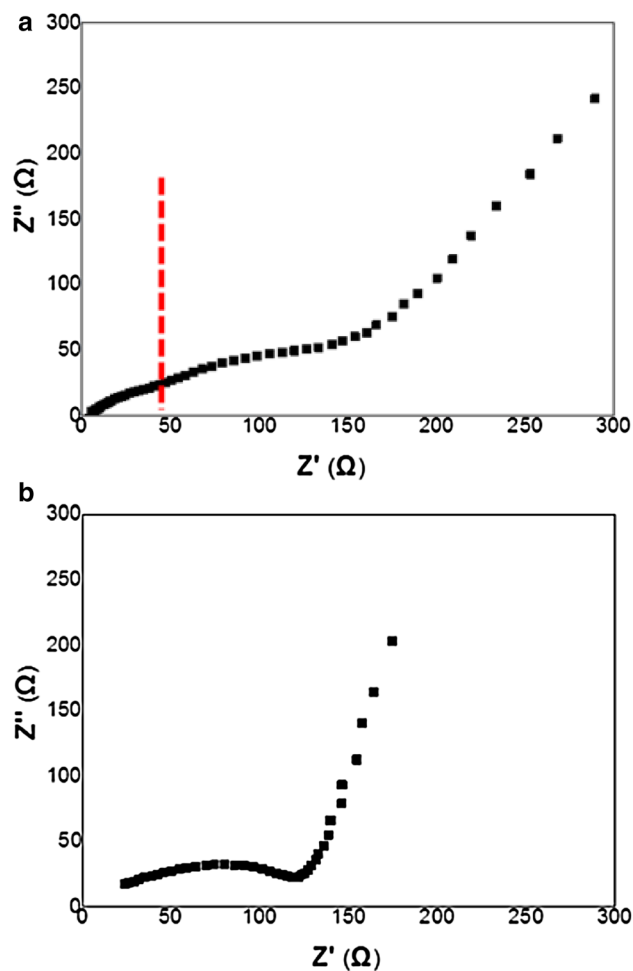


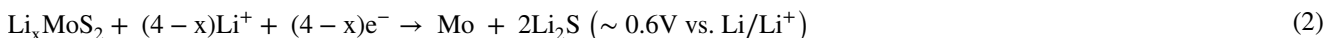
Fig. 9 AC impedance measurements of **a** uncalcined and **b** calcined $\text{MoS}_2\text{-TiO}_2$ electrodes at open-circuit potential of $\approx 3.0 \text{ V}$ (vs. Li/Li^+)

pseudocapacitive lithium ion insertion/extraction behavior in the anatase TiO_2 lattice, which are consistent with the previous reports [10, 28]. For the combined electrode, there are also specific electrochemical processes according to MoS_2 nanoparticles. Reactions take place at around 3–1.1 V during discharge can be expressed by [29]:



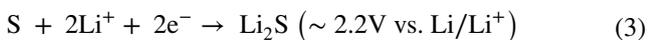
The theoretical specific charge capacity of this reaction is 167 mAh g^{-1} , which is related to the intercalation of one Li^+ per molybdenum atom [29].

The lower voltage plateau located at 0.6 V for the first discharge is attributed to the reversible conversion reaction of MoS_2 to Li_2S and metallic molybdenum through reactions (1) and then (2) [30, 31].



The theoretical specific charge capacity of reaction (2) is 669 mAh g^{-1} .

The reaction of the elemental sulfur and lithium usually happens at around 2.2 V, which can be described by Eq. (3) as follow [32, 33]:



Compared with the uncalcined electrode, the capacity retention of the calcined sample is higher, indicating that the calcined electrodes can possess higher reversibility than the uncalcined $\text{MoS}_2\text{-TiO}_2$ electrode.

Figure 8 shows the comparison of the rate performance between uncalcined and calcined $\text{MoS}_2\text{-TiO}_2$ electrodes at different current rates. It is obvious that the capacity of uncalcined $\text{MoS}_2\text{-TiO}_2$ electrode decreases rapidly with the increase of current density. But for calcined $\text{MoS}_2\text{-TiO}_2$ electrode, it shows a much higher specific capacity and much better rate capability. For example, at a current rate of 100 mA g^{-1} , the specific capacity of calcined $\text{MoS}_2\text{-TiO}_2$ electrode is about 570 mAh g^{-1} and at a high current rate of 1600 mA g^{-1} , which is around 380 mAh g^{-1} .

Table S1 summarizes the electrochemical performance

from the various literature sources. Interestingly, similar morphology can result in radically different electrochemical performance. By comparison, the superior rate capacity with excellent cycling performance of the 3D network $\text{MoS}_2\text{-TiO}_2$ anode with thermal treatment is better than that of most recently reported works on TiO_2 nanostructures [34, 35], TiO_2 hybrids composites anodes [36–45].

Fig. 10 SEM and magnified SEM images of (a, b) uncalcined $\text{MoS}_2\text{-TiO}_2$ and (c, d) calcined $\text{MoS}_2\text{-TiO}_2$ electrodes after 20 cycles at a current density of 800 mA g^{-1}

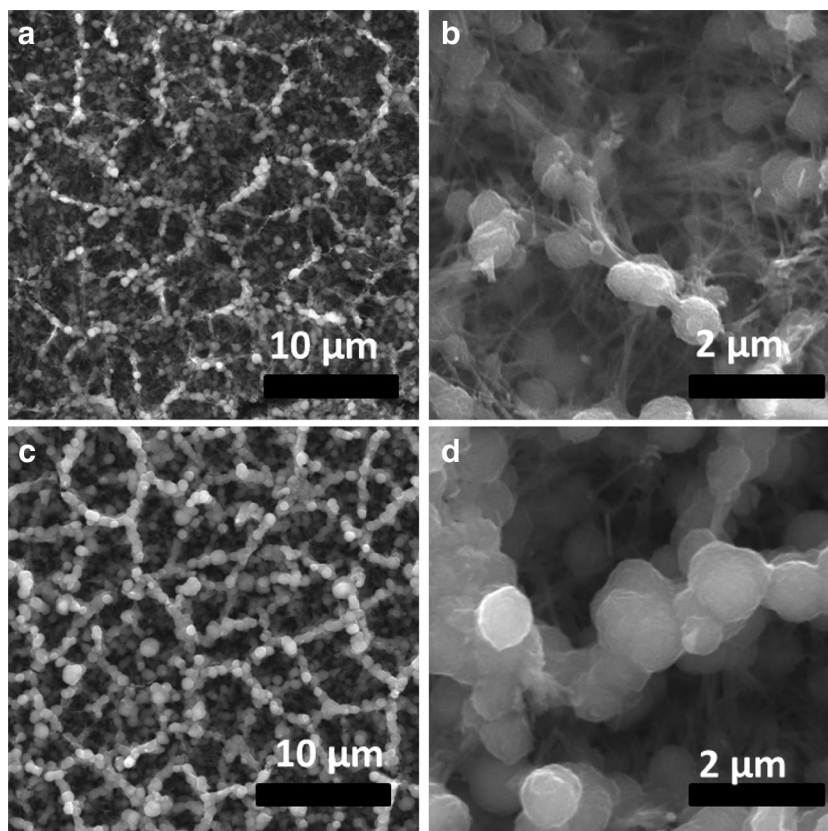


Figure 9 shows the typical impedance spectra of the pristine uncalcined and calcined $\text{MoS}_2\text{-TiO}_2$ electrodes at open-circuit potential (3.0 V vs. Li/Li^+). For the uncalcined $\text{MoS}_2\text{-TiO}_2$ electrode, the EIS diagram is composed of two depressed overlapped semicircles at high frequencies and a spike at low frequencies. Compared with it, the calcined electrode just shows one depressed semicircle at high frequencies. The high-frequency semicircle indicates the charge transfer resistance, while the spike at the low frequency is related to the Warburg impedance of long-range Li^+ diffusion [46]. The extra semicircle at high frequency for the uncalcined electrode may be caused by the resistance from the phase boundary between TiO_2 and MoS_2 [47]. For the calcined sample, this semicircle disappears, which further indicates the calcination can bring with a close connection between TiO_2 and MoS_2 and the phase boundary resistance can be largely reduced as result. In addition, the interception with real impedance axis for uncalcined $\text{MoS}_2\text{-TiO}_2$ is larger than that for the calcined sample, indicating that the close combination between TiO_2 and MoS_2 is favorable to the electrical conductivity. On the other hand, the increased slope in the low frequency end for the calcined $\text{MoS}_2\text{-TiO}_2$ composite might indicate that the electrochemical activity could be effectively improved after the calcination post-treatment. Therefore, we envisaged that the calcined electrode with a close combination between TiO_2 and MoS_2 would exhibit much better electrochemical performance than the uncalcined electrode.

In order to illuminate the superiority of the calcination, we analyzed the post cycling microstructure characterization by SEM images and energy dispersive X-ray spectra. As shown in Fig. 10, we can see the particles especially the TiO_2 nanowires reunion tends to occur easily in the uncalcined electrode and the particles can't remain an equal sized and uniform spherical particle as the starting materials. In contrast, for the calcined electrode, the MoS_2 still distribute evenly throughout TiO_2 nanowires after 20 cycles. Moreover, there is almost no change for the fracture and size of MoS_2 , which indicates that the calcined electrode material has a good cycling reversibility without obvious agglomeration and structure changes.

Figure 11 reveal that the EDS spectra of the uncalcined and calcined $\text{MoS}_2\text{-TiO}_2$ electrodes after cycling. According to the results as shown in Table 4, the mass ratio of S and Mo are determined to be 1.51 and 1.90 for the uncalcined and calcined samples, respectively. Compared with the uncalcined sample, the ratio of Mo and S element for the calcined sample is much closer to the stoichiometric ratio. This indicates the unnecessary sulfur of the uncalcined electrode can be consumed irreversibly. These above obtained results undoubtedly indicate that in order to improve the cycling stability, it's necessary to induce the calcination treatment to remove the extra sulfur, increase

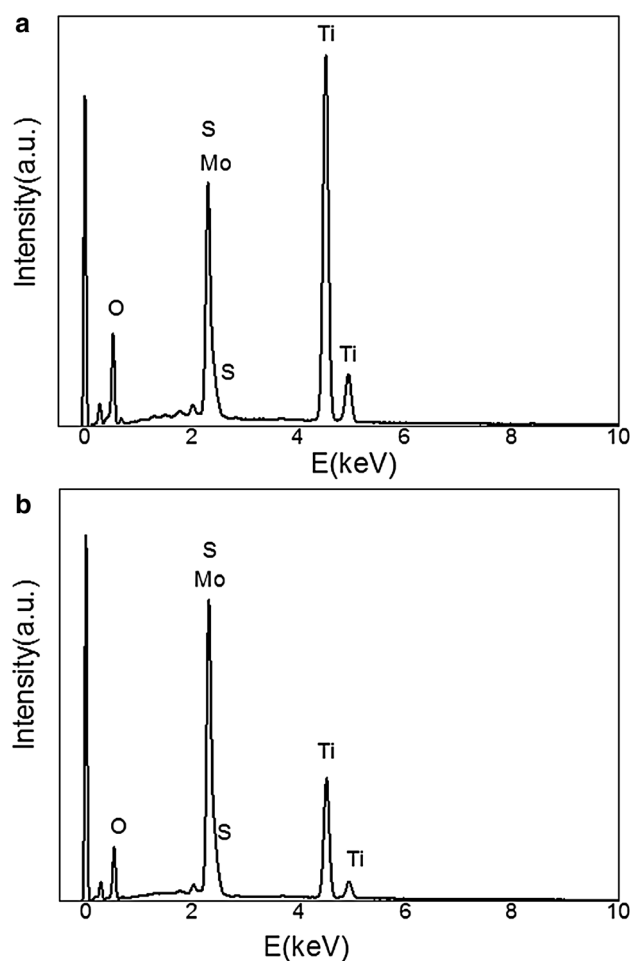


Fig. 11 EDS spectra of **a** uncalcined and **b** calcined $\text{MoS}_2\text{-TiO}_2$ electrodes after 20 cycles at a current density of 800 mA g^{-1}

Table 4 Elemental contents (in mol ratio) of S and Mo in the $\text{MoS}_2\text{-TiO}_2$ electrodes after 20 cycles at a current density of 800 mA g^{-1} obtained via EDS analysis

Element	Uncalcined sample	Calcined sample
S	1.51	1.90
Mo	1.00	1.00

the crystallinity of MoS_2 and promote the well connection between TiO_2 and MoS_2 .

4 Conclusion

We have developed an efficient approach to fabricate the $\text{MoS}_2\text{-TiO}_2$ binder free electrode with 3D network via a facile hydrothermal process. These unique hybrid nanostructures improve lithium storage properties and cycling stability. When being evaluated as an anode material for

LIBs, the second calcined MoS₂-TiO₂ electrode could retain a capacity of 361.5 mAh g⁻¹ with high capacity retention of 88.0% after 300 cycles at a high current density of 800 mA g⁻¹. These results reveal that the special 3D nano-network structure, the well-dispersed MoS₂ nanoparticles and the close connection between TiO₂ and MoS₂ play crucial roles in improving the capacity and rate performance of the MoS₂-TiO₂ electrode.

Acknowledgements The project was supported by National Natural Science Foundation of China (No. 51604132) and the State Key Laboratory of Physical Chemistry of Solid Surfaces of Xiamen University (201506).

References

- M. Selvamurugan, G. Hirankumar, S. Karuppuchamy, *J. Mater. Sci. Mater. Electron.* **27**, 9699 (2016)
- H.D. Chen, X.H. Hou, L.N. Qu, H.Q. Qin, Q. Ru, Y. Huang, S.J. Hu, K.H. Lam, *J. Mater. Sci. Mater. Electron.* **28**, 250 (2017)
- H.D. Liu, J.M. Huang, C.J. Xiang, J. Liu, X. L. Li, *J. Mater. Sci. Mater. Electron.* **24**, 3640 (2013)
- Y.C. Yang, X.B. Ji, M.J. Jing, H.S. Hou, Y.R. Zhu, L.B. Fang, X.M. Yang, Q.Y. Chen, C.E. Banks, *J. Mater. Chem. A* **3**, 5648 (2015)
- H.M. Wang, Y. Yan, G. Chen, *J. Mater. Chem. A* **3**, 10275 (2015)
- T. Song, U. Paik, *J. Mater. Chem. A* **4**, 14 (2016)
- L. Kavan, M. Gratzel, J. Rathousky, A. Zukal, *J. Electrochem. Soc.* **143**, 394 (1996)
- G. Sudant, E. Baudrin, D. Larcher, J.M. Tarascon, *J. Mater. Chem.* **15**, 1263 (2005)
- I. Moriguchi, R. Hidaka, H. Yamada, T. Kudo, H. Murakami, N. Nakashima, *Adv. Mater.* **18**, 69 (2006)
- X.Y. Pan, M.Q. Yang, X.Z. Fu, N. Zhang, Y.J. Xu, *Nanoscale* **5**, 3601 (2013)
- S.H. Nam, H.S. Shim, Y.S. Kim, M.A. Dar, J.G. Kim, W.B. Kim, *ACS Appl. Mater. Interfaces* **2**, 2046 (2010)
- N. Li, G.M. Zhou, R.P. Fang, F. Li, H.M. Cheng, *Nanoscale* **5**, 7780 (2013)
- B.L. He, B. Dong, H.L. Li, *Electrochem. Commun.* **9**, 425 (2007)
- V. Gentili, S. Brutti, L.J. Hardwick, A.R. Armstrong, S. Panero, P.G. Bruce, *Chem. Mater.* **24**, 4468 (2012)
- X.S. Peng, A.C. Chen, *Adv. Funct. Mater.* **16**, 1355 (2006)
- T.R. Thurston, J.P. Wilcoxon, *J. Phys. Chem. B* **103**, 11 (1999)
- T. Stephenson, Z. Li, B. Olsen, D. Mitlin, *Energy Environ. Sci.* **7**, 209 (2014)
- J.G. Wang, P. Zhang, X. Li, J. Zhu, H.X. Li, *Appl. Catal. B* **134–135**, 198 (2013)
- R. Sanjines, H. Tang, H. Berger, F. Gozzo, G. Margaritondo, F.J. Levy, *Appl. Phys.* **75**, 2945 (1994)
- H.W. Wang, P. Skeldon, G.E. Thompson, *Surf. Coat. Technol.* **91**, 200 (1997)
- V.O. Koroteev, L.G. Bulusheva, I.P. Asanov, E.V. Shlyakhova, D.V. Vyalikh, A.V. Okotrub, *J. Phys. Chem. C* **115**, 21199 (2011)
- C.H. Jiang, M.D. Wei, Z.M. Qi, T. Kudo, I. Honma, H.S. Zhou, *J. Power Sources* **166**, 239 (2007)
- Y. Ren, L.J. Hardwick, P.G. Bruce, *Angew. Chem. Int. Ed.* **49**, 2570 (2010)
- J.Y. Shin, D. Samuelis, J. Maier, *Adv. Funct. Mater.* **21**, 3464 (2011)
- L. Kavan, M. Gratzel, J. Rathousky, A. Zukal, *J. Electrochem. Soc.* **143**, 394 (1996)
- S.W. Kim, T.H. Han, J. Kim, H. Gwon, H.S. Moon, S.W. Kang, S.O. Kim, K. Kang, *ACS Nano* **3**, 1085 (2009)
- J. Wang, J. Polleux, J. Lim, B. Dunn, *J. Phys. Chem. C* **111**, 14925 (2007)
- L. Kavan, M. Kalbac, M. Zukalova, I. Exnar, V. Lorenzen, R. Nesper, M. Graetzel, *Chem. Mater.* **16**, 477 (2004)
- M.A. Py, R.R. Haering, *Can. J. Phys.* **61**, 76 (1983)
- G. Du, Z. Guo, S. Wang, R. Zeng, Z. Chen, H. Liu, *Chem. Commun.* **46**, 1106 (2010)
- K. Chang, W. Chen, L. Ma, H. Li, H. Li, F. Huang, Z. Xu, Q. Zhang, J.Y. Lee, *J. Mater. Chem.* **21**, 6251 (2011)
- K. Chang, W. Chen, *ACS Nano* **5**(6), 4720 (2011)
- Q. Wang, J. Li, *J. Phys. Chem. C* **111**, 1675 (2007)
- S. Brutti, V. Gentili, H. Menard, B. Scrosati, P.G. Bruce, *Adv. Energy Mater.* **2**, 322 (2012)
- S. Yoon, A. Manthiram, *J. Phys. Chem. C* **115**, 9410 (2011)
- L.G. Xue, Z. Wei, R.S. Li, J.L. Liu, T. Huang, S.A. Yu, *J. Mater. Chem.* **21**, 3216 (2011)
- Z.X. Yang, G.D. Du, Q. Meng, Z.P. Guo, X.B. Yu, Z.X. Chen, T.L. Guo, R. Zeng, *RSC Adv* **1**, 1834 (2011)
- Z.X. Yang, G.D. Du, Z.P. Guo, X.B. Yu, Z.X. Chen, T.L. Guo, R. Zeng, *Nanoscale* **3**, 4440 (2011)
- S. Li, M.Y. Wang, Y. Luo, J.G. Huang, *ACS Appl. Mater. Interfaces* **8**, 17343 (2016)
- W. Xu, T. Wang, Y. Yu, S. Wang, *J. Alloys Compd.* **689**, 460 (2016)
- X. Xu, Z. Fan, S. Ding, D. Yu, Y. Du, *Nanoscale* **6**, 5245 (2014)
- X. Li, W. Li, M. Li, P. Cui, D. Chen, T. Gengenbach, L. Chu, H. Liu, G. Song, *J. Mater. Chem. A* **3**, 2762 (2015)
- B. Guo, K. Yu, H. Fu, Q. Hua, R. Qi, H. Li, H. Song, S. Guo, Z. Zhu, *J. Mater. Chem. A* **3**, 6392 (2015)
- W. Zhuang, L. Li, J. Zhu, R. An, L. Lu, X. Lu, X. Wu, H. Ying, *ChemElectroChem* **2**, 374 (2015)
- J. Liao, B.A. De Luna, A. Manthiram, *J. Mater. Chem. A* **4**, 801 (2016)
- C.Y. Lee, H.M. Tsai, H.J. Chuang, S.Y. Li, P. Lin, T.Y. Tseng, *J. Electrochem. Soc.* **152**, A716 (2005)
- S. Skale, V. Doleček, M. Slemnik, *Corros. Sci.* **49**, 1045 (2007)